

Cosmic Ray Acceleration at the Forward Shock in Tycho's Supernova Remnant: Evidence from *Chandra* X-ray Observations

Jessica S. Warren,¹ John P. Hughes,¹ Carles Badenes,¹ Parviz Ghavamian,² Christopher F. McKee,³ David Moffett,⁴ Paul P. Plucinsky,⁵ Cara Rakowski,⁵ Estela Reynoso,⁶ and Patrick Slane⁵

ABSTRACT

We present evidence for cosmic ray acceleration at the forward shock in Tycho's supernova remnant (SNR) from three X-ray observables: (1) the proximity of the contact discontinuity to the forward shock, or blast wave, (2) the morphology of the emission from the rim of Tycho, and (3) the spectral nature of the rim emission. We determine the locations of the blast wave (BW), contact discontinuity (CD), and reverse shock (RS) around the rim of Tycho's supernova remnant using a principal component analysis and other methods applied to new *Chandra* data. The azimuthal-angle-averaged radius of the BW is $251''$. For the CD and RS we find average radii of $241''$ and $183''$, respectively. Taking account of projection effects, we find ratios of $1 : 0.93 : 0.70$ (BW : CD : RS). We show these values to be inconsistent with adiabatic hydrodynamical models of SNR evolution. The CD:BW ratio can be explained if cosmic ray acceleration of *ions* is occurring at the forward shock. The RS:BW ratio, as well as the strong Fe K α emission from the Tycho ejecta, imply that the RS is not accelerating cosmic rays. We also extract radial profiles from $\sim 34\%$ of the rim of Tycho and compare them to models of surface brightness profiles behind the BW for a purely thermal plasma with an adiabatic shock. The observed morphology of the rim is much more strongly peaked than predicted by the model, indicating that such thermal

¹Department of Physics & Astronomy, Rutgers University, 136 Frelinghuysen Road, Piscataway, NJ 08854-8019; jesawyer@physics.rutgers.edu, jph@physics.rutgers.edu

²Department of Physics & Astronomy, Johns Hopkins University, 3400 N Charles Street, Baltimore, MD 21218-2686

³Departments of Physics & Astronomy, University of California, Berkeley, CA 94720

⁴Physics Department, Furman University, 3300 Poinsett Highway, Greenville, SC 29613

⁵Harvard-Smithsonian Center for Astrophysics, 60 Garden Street, Cambridge, MA 02138

⁶Instituto de Astronomía y Física del Espacio, C.C. 67, Sucursal 28, 1428 Buenos Aires, Argentina

emission is implausible here. Spectral analysis also implies that the rim emission is non-thermal in nature, lending further support to the idea that Tycho’s forward shock is accelerating cosmic rays.

Subject headings: ISM: individual (Tycho) — supernova remnants — supernovae: general — X-rays: ISM

1. Introduction

With the clear detection of non-thermal X-ray synchrotron emission from the rims of the remnant of SN 1006 by Koyama et al. (1995), it was established that the shocks in supernova remnants (SNRs) can accelerate cosmic ray electrons to TeV energies. These energies are close to, but do not quite reach, the “knee” in the cosmic ray spectrum around 300 TeV. Since the work on SN 1006, several other SNRs have been found to emit X-ray synchrotron radiation, including Cas A (Allen et al. 1997), G266.2-1.2 (Slane et al. 2001), and G347.3-0.5 (Slane et al. 1999), implying cosmic ray shock acceleration may be common in young SNRs.

Still, much remains unknown or observationally unsubstantiated. How efficient is the acceleration mechanism? The amount of energy the shock puts into accelerating particles should be large (Decourchelle et al. 2000), but independent observational constraints on this are limited (e.g., Hughes et al. 2000). Are cosmic ray ions being accelerated? X-ray synchrotron radiation is evidence of relativistic cosmic ray electrons. Direct evidence of the presence of cosmic ray protons comes in the form of γ -rays via pion-decay (Ellison et al. 2005). This has not yet been conclusively detected, partly because such a signature is difficult to extract from the observations (see Baring et al. 2005; Malkov et al. 2005, and references therein). How does cosmic ray acceleration affect the dynamics of an SNR? The dynamical evolution of an SNR depends on the properties (e.g., explosion energy, mass of ejecta, ambient density) of its supernova (SN) and surrounding environment. These factors influence the rate at which the forward shock expands into the interstellar medium (ISM), where the contact discontinuity (which separates the SN ejecta from the swept-up ISM) lies, and the rate at which the reverse shock propagates into the ejecta. If the shocks are accelerating cosmic rays, particularly ions, their rates of propagation will be affected (Ellison et al. 2005).

In the 0.2-10 keV X-ray band where superb imaging of SNRs is possible using *Chandra*, the key to addressing these questions lies in cleanly separating regions whose emission is dominated by featureless spectra from other regions that are line dominated. In all but the most exceptional cases, one can identify the dominant emission processes in these two types

of regions to be X-ray synchrotron radiation or thermal radiation from shock-heated ejecta or ISM, respectively. With the power to discriminate where these different processes occur in an SNR, one can identify the sites where electrons are being accelerated to high energies and where the shocked material (both ejecta and ambient) is situated. With knowledge of the locations of the blast wave and contact discontinuity one constrains the dynamical state of the remnant and can then investigate what role, if any, cosmic ray acceleration plays.

In this article, we demonstrate the separation of featureless-dominated and line-dominated emission in the remnant of SN 1572 (hereafter Tycho) using the results of a principal component analysis (PCA). PCA is a mathematical operation that reduces the dimensionality of a dataset. This is accomplished by finding new variables to characterize the data that are linear combinations of the original variables. These new variables, or principal components, are chosen such that they maximize the variance of the data. For Tycho, our data consist of the spectra of thousands of spatial regions in the SNR. Our original variables are spectral channels, or energy bands.

The analysis in our paper is the first application of PCA to data from an SNR. Tycho, however, has been studied extensively with other means. It is widely believed to be the remnant of a Type Ia supernova (SN Ia). Tycho’s forward shock is filamentary and shows featureless X-ray emission in the *Chandra* band, of which some fraction is likely to be non-thermal (Hwang et al. 2002). Optical observations reveal thin Balmer-dominated filaments in the north and east of the remnant (Smith et al. 1991; Ghavamian et al. 2001). In the radio, Tycho shows a limb-brightened shell and a thicker, inner shell (Dickel et al. 1991). These authors and, more recently, Katz-Stone et al. (2000) found that the radio emission is consistent with the acceleration of cosmic ray electrons by the forward shock. Reynolds & Ellison (1992) specifically modeled the non-linear first-order Fermi acceleration mechanism (also called diffusive shock acceleration, DSA), which is believed to be the process by which the shock accelerates cosmic rays. They found good agreement between the model and the radio spectrum of Tycho. Ellison (2001) compared a model of DSA to Tycho’s combined radio and X-ray spectrum, including limits from γ -ray observations. He found that the shock can accelerate particles up to TeV energies, whose synchrotron signature should be detected in the X-ray band. Additionally, hard X-rays out to \sim 20 keV have been detected in Tycho with the *Ginga* satellite (Fink et al. 1994). The spectrum at these energies cannot be fit with a single bremsstrahlung component, but requires a second, “flat” component to fit the emission.

The ejecta of Tycho, only visible in the X-rays, are spread throughout the interior in a clumpy shell-like distribution and are mainly Si- and Fe-rich (Hwang et al. 1998; Decourchelle et al. 2001). The Fe emission in Tycho appears to be stratified; the Fe L emission peaks at

a larger radius than the Fe K emission (Hwang & Gotthelf 1997). A hot Fe component is required to reproduce the flux in the Fe K α line in the integrated spectrum, implying there is a temperature gradient in the ejecta (Hwang et al. 1998).

The distance to Tycho is estimated to be between 1.5–3 kpc (Smith et al. 1991), depending on the method used. Our main conclusions are based on ratios of observed radii and are therefore distance independent. When quoting results in physical units, we explicitly state the distance value used (2.3 kpc).

The plan of our paper is as follows. In §2 we describe our observations and the PCA technique. The results of the PCA allow us to locate the contact discontinuity, which we do in §3 along with locating the blast wave. In §4 we examine the azimuthal variation of radial fluctuations of the contact discontinuity via a power spectrum analysis. We examine the radial morphology of the rim in §5. To round out our discussion of the fluid discontinuities in Tycho, in §6 we determine the location of the reverse shock. Finally, we discuss our results in §7 and summarize the paper in §8.

2. Observations and Techniques

We observed Tycho with the *Chandra* Advanced CCD Imaging Spectrometer (ACIS-I) detector on 2003 April 29–30 for \sim 150 ks (ObsID 3837) in timed exposure mode. All four chips were active, the aimpoint was located at the SNR’s geometric center, and the full 8' diameter extent of Tycho was imaged. Unfortunately, the instrument was in dither mode (which ensures that no single portion of the image falls on a bad pixel for the entire observation) for only the latter 68 ks of the exposure. However, the lack of dithering for roughly half the observation had no significant impact on our analysis. We applied standard reduction techniques to the events, filtering on grade (retaining the usual values 02346) and bad pixels, and eliminating times of high background. We removed pixel randomization and applied the time-dependent gain correction on an event-by-event basis. After all processing, the final exposure time was 145.2 ks.

2.1. Three-color Image

Figure 1 (top left) is a composite of three X-ray energy bands that are dominated by emission from Fe L-shell (red), Si K-shell (green), and high energy (4–6 keV) continuum (blue). The blue component is spectrally hard and featureless. It predominates at the outer rim in the form of thin, moderately high surface brightness filaments that can be traced

continuously for nearly 180° around the rim from the north to southwest. This emission also spreads throughout the interior. Two features in particular stand out: a small arc in the southeast, and a larger, fainter arc that runs northward from the southeast. These are possibly more of the filamentary structures at the rim that are just seen in projection. There are also two more knot-like structures in this energy range in the southwest, slightly behind the rim (one of which was noted by Hwang et al. 2002). The “fleecy” green component is rich in Si and S and generally fills the interior. At several locations it extends to the edge of the SNR, breaking through the blue rim emission. The red component is more Fe-rich and appears particularly enhanced in a small region on the eastern rim (first noted by Vancura et al. 1995) and a more extensive region interior to the Si-rich zone in the northwest. Both the red and green components are more knot-like in structure, as opposed to the filamentary nature of the blue component.

2.2. PCA Technique

Already we see from the 3-color image that emission from the rim, or forward shock, stands out in the 4–6 keV continuum range, while the interior emission is line-dominated. It seems likely that judicious use of the 3-color image or some combination of ratio images would allow us to separate the forward shock (ISM) emission from the interior (ejecta) emission. Similar problems have presented themselves in many of our previous studies with *Chandra*, and so rather than pursue a limited *ad hoc* approach here just for Tycho, we decided to investigate principal component analysis (PCA), which is a general mathematical technique that is quantitative, rigorous, and less subject to observer bias.

We present here a brief summary of our application of PCA to Tycho; an in-depth account and further motivation will be given elsewhere (Warren & Hughes 2005). A mathematical description of PCA can be found in Murtagh & Heck (1987). We extracted, from small regions across the entire remnant, a large number of spectra in 12 broad spectral channels that were chosen to isolate important spectral features (e.g., the three energy bands in the color composite, see Table 1). These spectra can be considered as points in a 12-dimensional space, whose axes correspond to the counts in each spectral channel. PCA is a mathematical operation that identifies a new set of 12 axes along which the variance of the data points is maximized. These new axes, called principal components, are a rank-ordered set of spectral templates that quantify both the amount and type of spectral variation within the data. In other words, the principal components are linear combinations of the original 12 spectral channels. The top right image in Figure 1 represents one linear combination of images made in those original 12 spectral bands. The weight factors quantifying the con-

tribution from each individual band image are determined from the entire dataset through the well-defined mathematical process of PCA. The image is conceptually analogous to the hardness ratio images that many X-ray astronomers use to identify spectral variations with position. The PCA is a significant generalization of that technique, since it uses the entire spectral range of a dataset.

We found that the Tycho spectral data points, when projected onto the new principal axes, were distributed in a well-behaved manner: the points were spread out along, and very nearly parallel to, the principal axes. The spread of data points along one of the new principal axes need not correspond uniquely to variations in a single physical parameter. In our application here, however, we found that the first principal axis, which accounts for $\sim 43\%$ of the total spectral variation, allows for a simple physical interpretation. The top right panel of Figure 1 shows the projection of the *Chandra* data onto this first principal axis (hereafter PC1). Comparison with the color image suggests that regions appearing light-colored in the PC1 image correspond to the “fleecy” Si- and Fe-rich emission, while the dark regions correspond to the hard continuum emission.

2.3. Spectra

To further support our interpretation of PC1 we extracted and studied the spectra from a large number of regions in Tycho (in the following we present and discuss only a representative subset of these spectra). The spectra from three regions along the N, S, and SW rim, corresponding to extreme values of PC1, are plotted in Figure 2 (top panel). They were well-fitted by absorbed power-law spectral models ($\chi^2_{reduced} \sim 0.8$) with parameter values in the range $N_{\text{H}} = (5.8 - 6.9) \times 10^{21} \text{ cm}^{-2}$ and $\alpha_P = 2.67 - 2.71$. Pure bremsstrahlung models result in equally good fits with parameter value ranges of $N_{\text{H}} = (3.9 - 4.8) \times 10^{21} \text{ cm}^{-2}$ and $kT = 2.1 - 2.2 \text{ keV}$. We discuss the nature of the emission mechanism for the rim in §7.4.1 below. Here, our intent is simply to demonstrate that extreme values to one direction along the PC1 axis (i.e., the dark portions of the PC1 image) correspond to featureless-dominated spectra that are mainly distributed around the rim of Tycho.

We extracted spectra from the reddish and yellowish regions in the southeast in Figure 1 (top left), which also correspond to light portions of the PC1 image. These are plotted in Figure 2 (bottom panel) and clearly show that the red region is Fe-rich and the yellow region is Si-rich. Although we do not show them here (a more detailed analysis of the ejecta is left to Hughes et al. 2005), we extracted several more spectra from various “knots” around the remnant that appear light-colored in the PC1 image. All of these are line-dominated, mainly by Si and S K α . It is thus clear that the light portions of the PC1 image correspond

to metal-rich thermal spectra. The PCA technique therefore has given us a clear delineation between the two main spectral types in Tycho: the featureless rim emission and the metal-rich thermal emission in the remnant interior. From our PCA technique, we note as an important addition that thermal emission from material with normal solar-type composition is not a major spectral type in Tycho.

Based on its morphology, the featureless component must be emission from the blast wave (BW). As we move in from the rim, Si and S line emission becomes more prominent. We interpret this thermal emission appearing behind the rim as shocked ejecta, rather than the progression of the ionization state behind the BW (e.g., Hwang et al. 2002). Moving in from the rim, the ejecta become less diluted with the surrounding shocked ambient medium, simply due to geometric projection. The ejecta shell is clumpy and patchy. In the interior there is a correlation between the X-ray intensity (Figure 1 top left) and PC1 image: where the overall brightness is low, the spectral character shifts toward the featureless type and vice versa. This is likely the effect of the projection of the BW and ejecta shells that vary in thickness and intrinsic intensity across the line of sight. This interpretation allows us to determine the location of the contact discontinuity (CD).

3. Tycho’s Blast Wave and Contact Discontinuity

We associate the maximum radial extent of the *broadband* X-ray emission with the location of the BW, regardless of its spectral character. This ensures that the BW radius is always greater than or equal to the CD radius. To determine the position of the BW, we first blocked our image to a scale of $0''.984$ per pixel. At a given azimuthal angle, we extracted the radial surface brightness profile from the broadband image and determined the radius where the profile first exceeded 8 cts pixel^{-1} moving in from the outside (see the top panel of Figure 3). We repeated this for angular steps of 1° around the entire SNR. The surface brightness value used ($5.7 \times 10^{-5} \text{ cts s}^{-1} \text{ arcsec}^{-2}$ or roughly 7 times the background) provided a compromise in denoting the BW radius between faint regions, as in the north and southeast, and bright regions, as in the northwest and east. At any given azimuthal angle, we expect the accuracy in measuring the position of a specific contour level (i.e., the location of the BW) to be of order the width of the point-spread-function (PSF) divided by the square root of the number of counts at that contour level. This evaluates to $\sim 1''/\sqrt{8} \sim 0''.3$ in our case. The BW radius as a function of azimuthal angle is plotted as the black curve in Figure 4. The center for this determination (R.A.= $00^{\text{h}}25^{\text{m}}19^{\text{s}}40$, decl.= $+64^\circ 08'13''.98$) was chosen to minimize the ellipticity of the BW and is used as the center throughout.

We determined the location of the CD from the value of PC1 (i.e., the level of “dark-

ness” in the PC1 image) that discriminates between the outermost ejecta and BW emission. This was obtained from the distribution of PC1 values, which has a well-defined peak (see Figure 5). This peak comes from the large number of pixels associated with a light yellow color in the PC1 image, which we established as being thermal in nature. The distribution around the peak is well-fit by a Gaussian with $\sigma = 0.028$ (the red curve in Figure 5), although there is an excess of PC1 values corresponding to pixels in which the emission is dominated by the featureless component. We found the PC1 value needed to discriminate between ejecta (thermal) and blast wave (featureless) emission by first using the Gaussian to represent the thermal distribution *alone*, then calculating the PC1 value lying 3σ away from the peak on the side representing featureless emission. Pixels with PC1 values lying below this 3σ threshold are unlikely to be dominated by thermal emission.

To mark this position on the remnant, we took the intensity-weighted average of PC1 values for regions of size 1° ($\sim 4''$ at the rim) in azimuth by $3''$ in radius. Moving in from the rim in $1''$ steps, we found the radius where the average PC1 value first crossed the 3σ threshold. We took this to be the radius of the CD. A contour representing this delineation is shown in the PC1 image (Figure 1), and a radial profile for a 1° -wide wedge is shown in the middle panel of Figure 3. We also looked at the contours corresponding to PC1 values 2σ and 4σ away from the peak and found no significant qualitative differences. We therefore use the 3σ criterion for determining the CD in what follows, unless otherwise stated.

It is important to note that in determining the location of the CD with the PCA technique we have utilized information from the *entire* spectral range. This is in contrast to other methods which rely on a single line (e.g. Si K α) to locate the CD.

We find the CD is close to the BW; the average radius of the CD ($241''$) is 96% that of the BW ($251''$). If we use the 2σ and 4σ radii, we find the CD radius is 94% and 98% of the BW radius, respectively. In Figure 4 we plot the CD radius vs. azimuthal angle. One can see that the ejecta extend out as far as the BW in discrete clumps at several azimuthal angles (e.g., 40° – 65° , 95° , 110° , 195° , and 360°). These clumps are Si-rich, with the exception of the Fe-rich knots between 105° and 115° . Figure 4 also indicates that the CD is much more highly structured than the BW on small angular scales. We quantify this last statement by examining the power spectrum of radial amplitude fluctuations.

4. Power Spectrum

The tabulated functions of radius vs. azimuthal angle for the BW and CD were each decomposed in a harmonic sequence, resulting in amplitudes and phase values for each of

180 trigonometric basis functions used. The power spectra (the square of the amplitudes) as a function of wavenumber (defined as $k = n/R_{\text{ave}}$, where n is the order of the trigonometric function and R_{ave} is the average radius) are shown in Figure 6 for the BW (black) and CD (green). The power peaks at low wavenumbers (long wavelengths) for both the BW and CD and falls off at higher values. We find no evidence for periodicity as suggested by Velázquez et al. (1998). Each power spectrum is well described by a power law (as plotted on Figure 6); we find $P \sim k^{-1.5}$ (CD) and $P \sim k^{-2.2}$ (BW). The single wavenumber with the largest power for the CD corresponds to $n = 6$ (or a wavelength in the azimuthal direction of 60°). The amplitude of this component is 3.3% of the average radius; the BW shows nearly the same value. The minimum observed power in the BW spectrum ($\sim 0.003 \text{ arcsec}^2$) corresponds to radial fluctuations with an amplitude of $\sim 0''.3$. Since these arise from both intrinsic and random (noise) variations in the measured position, we conclude that the accuracy in the BW radial positions is on average better than $0''.3$, consistent with the uncertainty estimated above.

The lack of a preferred scale length and the predominance of power at low wavenumbers in the CD is qualitatively consistent with expectations for structure driven by the Rayleigh-Taylor and Kelvin-Helmholtz instabilities (e.g., Chevalier et al. 1992). At higher wavenumbers the CD shows nearly an order of magnitude more power than the BW, indicative of instabilities acting at the CD. The level of power at low wavenumbers is nearly the same for the BW as the CD, even though the former is not subject to instability. However, as the direct observation of ejecta at the BW makes clear, some (and perhaps most) of the BW's low order power is a result of these ejecta protrusions, although it is possible that additional power comes from environmental factors.

It is our hope that, in the not-too-distant future, multi-dimensional hydrodynamical calculations of SNR evolution will have the resolution to be able to produce radial power spectra similar to those we present here from the observations. Comparison of observed and simulated power spectra may yield insights into the fluid properties of the ejecta.

5. Radial Morphology at the Rim of Tycho's SNR

In the previous sections, we investigated the global structure of Tycho's rim as a function of azimuthal angle. In order to gain more insight into the precise nature and origin of this emission, here we examine in detail the radial morphology of the rim. We began with the 4–6 keV band image, which is largely uncontaminated by line emission. In selecting regions we avoided parts of the rim that were contaminated by ejecta (identified using our 3σ PC1 criterion) or where the edge was clearly structured (i.e., from multiple overlapping rims

projected on top of each other). This left us with seven separate azimuthal regions covering $\sim 34\%$ of the entire rim (see Figure 1, bottom left). Rather than extract a typical radial profile by summing over a range of azimuthal angles for a fixed set of radial bins, we accounted for the azimuthal rippling of the BW location within a given extraction region. First, the azimuthal angle of each pixel in the extraction region was determined. With this angle it was possible to look up the location of the BW in radius (i.e., from Figure 4) and determine the radial distance of the pixel behind (or ahead of) the BW. The number of detected X-ray events in the pixel was then added to a radial profile binned with respect to the BW location. A radial profile of the exposure map (produced using standard CIAO software) was made in the same way and then divided into the count rate profile. The resulting surface brightness profiles for the seven regions are plotted as the crosses in Figure 7. Note that each profile in the figure has been plotted so that the mean BW radius for the azimuthal region is approximately correct. In all cases, while moving inward, the profiles rise rapidly from the background level to a peak and then fall-off in brightness further in toward the interior. The widths of the rim as seen here in projection are quite narrow, of order only a few arcseconds, as previously noted by Hwang et al. (2002) and Bamba et al. (2005).

5.1. Rim Widths from Spherical Shell Models

Here we consider two simple models for the intrinsic three-dimensional structure of the rims. Both cases assume the X-ray emission comes from a geometrically thin spherical shell. In the first case the emissivity is considered to be uniform within the shell; the other model, following Berezhko & Völk (2004), assumes the emissivity falls off exponentially behind the shock, which is defined to be the outer radius of the shell. The relevant parameters are the outer radius of the shell, the shell thickness (or the 1/e length of the exponential profile), an intensity scale factor, and a background level (assumed spatially uniform). The models are projected to the plane of the sky and convolved with the *Chandra* point-spread-function (PSF) appropriate to each region. PSF simulations were generated using the *Chandra* Ray Tracer (ChaRT)¹ for a photon energy of 4.8 keV (the mean weighted energy in the 4–6 keV band). The input location to ChaRT was taken as the center of each azimuthal region at the BW. The FWHM radial widths of the PSF profiles varied from $1''$ to $2''$. Our fits improved substantially when convolution with the PSF was included (especially for the exponential profile), clearly demonstrating the value and importance of including this in the fitting process.

¹ChaRT and MARX are available at: <http://asc.harvard.edu/chart/index.html>

We plot the best-fit uniform-emissivity projected shell models convolved with the PSF as the solid histograms in Figure 7. Nearly all of the rim profiles are well-described by this simple model, although in two cases (regions covering azimuthal angles 312° – 318° and 273° – 289°) the observed surface brightness profiles are more limb-brightened than the model. This cannot be solved by merely reducing the intrinsic thickness of the shell model since this causes the width of the projected profile to decrease, thereby degrading the fit. We surmise that these azimuthal locations may be places where our assumption of a spherically symmetric shell breaks down. The thickness of the shells range from $2''.0$ – $5''.7$ for the uniform emissivity case.

For the case where the emissivity falls exponentially with distance from the shock front we use the approximate formula² given by Berezhko & Völk (2004) for the projected profile. The quality of the fits here is just about as good as in the previous case, although the best fit “widths” (i.e., $1/e$ lengths) are much smaller and range over values of $0''.4$ – $2''.9$.

Since neither the uniform nor exponential profile cases is a clear winner in terms of quality of fit and given the absence of any strong astrophysical motivation to support one or the other, we will carry both sets of width values in our subsequent discussions and calculations.

5.2. Rim Morphology for Shocked Plasma at the Blast Wave

The extremely thin filaments around the outer rim of Tycho, first noted by Hwang et al. (2002), are not what we would expect from standard adiabatic hydrodynamical evolutionary models. Our expectation from such models is for a much thicker region of thermal emission, determined by the profiles of gas density, temperature, and ionization conditions behind the BW. These thermodynamic quantities themselves depend on the specific physical conditions and evolutionary state of the remnant. Although the gas density behind the BW is highest right at the shock front, other thermodynamic quantities evolve with time (i.e., distance behind the BW) and may not conspire to produce peak emissivity near the rim.

To investigate this quantitatively we have produced surface brightness profiles behind the BW for a purely thermal plasma with an adiabatic shock. We applied the hydrodynamic and ionization codes described in Badenes et al. (2003) to the shocked ambient medium (AM). These assume the unshocked AM has a constant density of $1 \times 10^{-24} \text{ g cm}^{-3}$ and

²In Berezhko & Völk (2004) the correct relation appears as eqn. 6. There are typographical errors in the same relation presented as eqn. 1 in Völk et al. (2005).

solar composition, and we varied the amount of collisionless electron heating at the BW. These calculations are very similar to those described in Borkowski et al. (2001) - the reader is referred to that paper for details. For the examples presented here, we used the structure of the BW at the age of Tycho, as extracted from a simulation where the SN Ia explosion model was a delayed detonation with a kinetic energy of 1.16×10^{51} erg (model DDTc from Badenes et al. 2005) - but such details do not affect the results for the profile of thermal emission behind the BW.

In Figure 8 (top panel) we show two profiles that span the range of observed shell thicknesses overlaid with the profiles from these calculations. The model profiles are not limb-brightened on the scale presented and do an exceptionally poor job of describing the observations. Given that the geometric shell models are such a good description of the data, only a modest fraction of the rim emission could come from a component that is distributed morphologically like shocked AM. In lieu of a detailed morphological model that explains the observed profile, as a first approximation, we use a joint model consisting of the sum of the profiles of the thermal emission and a purely geometric thin shell. The bottom panel of Figure 8 shows our joint model fits with the allowed upper limit (90% confidence) to the thermal emission from the shocked AM shown as the lower dashed histograms. For the somewhat thicker profile (left side) as much as 33% of the integrated rim emission could come from the same thermal component. This limit is reduced to only 9% for the thinner profile (right side).

6. Tycho’s Reverse Shock

Although our focus has been on the location of the BW and CD and the emission from the region between them, we wish to round out our investigation of the fluid discontinuities in Tycho by locating the reverse shock (RS). To do this, we take our cue from models of SN Ia explosions. SNe Ia are thermonuclear explosions involving C and O white dwarfs (Hillebrandt & Niemeyer 2000). For many years, theoretical models of SN Ia explosions relied on one-dimensional calculations, involving stratification in the ejecta: Fe-peak elements are interior to Si, S and other intermediate mass elements. More recently, three-dimensional models of SN Ia explosions have appeared, which result in a very efficient mixing of all the elements throughout the ejecta (Reinecke et al. 2002; Gamezo et al. 2003; García-Senz & Bravo 2005). However, it is unclear whether these models can explain the fundamental properties of the optical spectra of SNe Ia (Baron et al. 2003; Bravo et al. 2004), as well as reproduce the X-ray spectra of SNRs. Specifically, they predict similar spectral properties for the Si and Fe emission in the shocked SN ejecta (Badenes et al. 2005). This is in conflict with the

results of Hwang et al. (1998) who showed from Tycho’s integrated X-ray spectrum that a component of Fe emission with a hotter temperature than that of the bulk Si emission was required to reproduce the flux in the Fe $K\alpha$ line. Additionally, observations show that this Fe $K\alpha$ emission peaks interior to that of Fe L and Si (Hwang & Gotthelf 1997; Decourchelle et al. 2001; Hwang et al. 2002), suggesting that there is a temperature gradient through the ejecta (cool near the contact discontinuity, hottest near the reverse shock). Badenes et al. (2005) also provided a theoretical interpretation for the hot Fe in the interior, with incomplete collisionless electron heating at the reverse shock and the subsequent evolution of temperature toward the CD in SNe Ia. Based on this evidence, we take the point of view that the Fe $K\alpha$ emission comes from the innermost portion of the shocked ejecta and its inner edge therefore denotes the location of the reverse shock (RS).

Figure 1 (bottom right) shows the continuum (4–6 keV band) subtracted Fe $K\alpha$ line image (which contains ~ 15000 counts in total). Over all but a portion of the eastern side, the image is circularly symmetric and clearly limb-brightened. We extracted radial profiles from within 12° -wide wedges as a function of azimuthal angle around the entire SNR and fit each profile independently with simple projected shell models. These models are purely geometric and assume a spherically-symmetric, uniform density shell. The inner and outer radii are the relevant fitting parameters. Fits with 1, 2, and 4 shell components were tried; the location of the innermost radius, i.e., the location of the RS, was insensitive to the number of components. The two-component shell model resulted in generally good fits ($\chi^2_{reduced} \sim 1$) for azimuthal angles over 0° – 48° and 168° – 360° with modest uncertainties in the RS radius. We find an average (error weighted) radius for the RS of $183''$.

The ratio of the RS to BW radii over these azimuthal ranges is 72% and only increases to 73% if we use the average BW radius from the entire 360° . In the following we will assume that the average radius for the RS can be extrapolated to the full 360° . Figure 4 shows the RS radius as a function of azimuthal angle as the purple histogram, with 90% error bars overplotted. The innermost contour on Figure 1 (bottom right) indicates the location of the RS. It clearly traces the peak of the Fe $K\alpha$ line surface brightness around the remnant, which agrees with what is expected for the projection of a thin shell. In the east, although the shell model describes the profiles accurately, the inner radius is not well constrained by the fits and the errors on this quantity are much larger than elsewhere (factors of 2 or more). We have chosen to exclude these regions from our further analysis. The coincidence of the bright Fe/Si knots and the seeming “gap” in the RS on the eastern limb has not escaped our attention. We will address this curious morphology in future work.

7. Discussion

Three key results on Tycho’s SNR that address the spectral character of the blast wave emission, its fine scale morphology, and the radial positions of the blast wave, contact discontinuity, and reverse shock emerge from the preceeding sections. Here we consider the implications of these results for the nature of Tycho’s SNR and show that all three observables are consistent with a single specific intrepretation.

7.1. Biases and Errors in the Locations of the Fluid Discontinuities

Before proceeding to use the relative radial positions of the fluid discontinuites to constrain the dynamical state of the remnant, we must first be certain that the projected radii we measure are unbiased estimates of the “true” radii. Let us first consider the effect of geometric projection. If the blast wave and ejecta were perfectly smooth and symmetric shells of emission, then the radii we observe would be close to the true radii. In practice, this is not the case; the shells of emission are highly structured. The true average radius lies somewhere between the maximum and minimum radial extent of the protrusions and indentations around the shell. Projecting a highly structured shell onto the plane of the sky tends to favor protruding parts of the shell. Therefore, the average radius we measure in projection is an overestimate of the true average radius.

We have done simple simulations using our power-spectrum analysis (§4) to quantify the amount of bias from projection for the BW and CD radii. According to these simulations, our observed values for both positions are over-estimated by $\sim 3\%$ and $\sim 6\%$, respectively. Another estimate for the bias in the CD radius comes from examining the hydrodynamical evolutionary models of Wang & Chevalier (2001). In these two-dimensional calculations, the Rayleigh-Taylor instability at the CD allows fingers of ejecta to protrude beyond the average CD radius. Wang & Chevalier (2001) find that the maximum extent of these fingers can extend to 87% of the BW radius, while their one-dimensional simulations place the CD at 77% of the BW radius. The true average radius of the CD should lie between these extremes. If the average CD radius we measure in projection is dominated by the maximum extent of the fingers, then we would be over-estimating the true CD radius by $\sim 5\%$.

The RS radius we quote from the shell fits to the Fe $K\alpha$ image is also likely to be over-estimated. We know that there is Fe $K\alpha$ emission at least down to the radius we quote; however, there may be even more shocked ejecta further in that is simply too faint to detect. Specifically our main concerns are the amount of radial variation in the intrinsic Fe $K\alpha$ emissivity through the ejecta shell (we assume uniform emissivity in our fits), and the

precise location of the reverse shock relative to the Fe K α emission. To assess these effects we again turn to the hydrodynamical simulations presented in §5.2, only now we consider the Fe ejecta emission. From the simulations we produced model Fe K α surface brightness profiles under a range of conditions. The profiles were generated on radial bins and with simulated errors to match the data (e.g., lower panel of Figure 3). These were then fit with the uniform shell model in the same way as the data profiles. Comparing the fitted inner edge of the shell model with the precisely known location of the RS from the simulation allowed us to estimate the bias. As expected the shell fits over-estimated the true radius of the RS, but the bias factor was modest: it varied from 1%–3% for plausible model conditions up to a factor of 8% for a more extreme case. To be conservative we use a RS bias factor of 5%.

We are now in the position to convert our measured projected average radii for the BW, CD, and RS ($251'' : 241'' : 183''$ or equivalently $1 : 0.96 : 0.73$ when scaled to the BW) to relative values that more accurately reflect the “true” radii of these surfaces. As shown above the relative bias between the CD and BW is $\sim 3\%$, and between the RS and BW the bias is $\sim 2\%$. Including these correction factors, our best estimate for the true relative radii become $1 : 0.93 : 0.71$ (BW : CD : RS). We use these values for the remainder of the discussion. (Note that Seward et al. (1983), using only the *Einstein* broadband X-ray image, derived qualitative estimates for the locations of the fluid discontinuities that are similar to the values from our detailed analysis.)

One final point about the radii concerns their uncertainty. The error on the BW radius is negligible compared to the errors on the radii of the CD and RS. An estimate for the error on the CD radius comes from comparing the 2σ and 4σ average radii (see §3) with the nominal 3σ value. This prescription gives an error on the relative CD radius of $\pm 2\%$. Our shell fits resulted in uncertainties on the RS radii for each of 20 separate 12° wide azimuthal sectors that varied from $4''$ to $17''$. If each sector is assumed to provide an independent estimate for the RS radius, then the formal error on the average RS radius would be $\sim 1''.4$, which is rather optimistic. To be conservative we take the average uncertainty from the separate fits, $7''.6$. This corresponds to an error on the relative RS radius of $\pm 3\%$.

7.2. Adiabatic Hydrodynamical Models

There are only a handful of references in the literature that present numerical values for all three of the radial locations we have measured in Tycho. Hamilton et al. (1986) found relative radii of $1 : 0.86 : 0.83$ at the dynamical age of Tycho for uniform density ejecta in an undecelerated blast wave, while Wang & Chevalier (2001) found $1 : 0.77 : 0.66$ for ejecta

with an exponential density profile. Neither of these simulations comes close to matching our observed CD:BW ratio of 0.93. Since the ratio of radii depends on the density profiles in the ejecta and ambient medium and additionally varies with time for a given set of profiles, we perform a more detailed comparison between our observed values and the predicted radii for the BW, CD and RS from the hydrodynamical simulations of Badenes et al. (2003) and Badenes et al. (2005). These models utilize realistic density profiles for the ejecta obtained from SN Ia explosion models. The ambient medium is assumed to be uniform.

The three curves in Figure 9 show how the ratio of radii vary with time for one specific SN Ia explosion model (case DDTc from Badenes et al. 2005). The horizontal axis in this figure is the normalized time, t' . To obtain the actual physical age of the remnant one multiplies t' by the factor

$$T' = \frac{M_{ej}^{5/6}}{[(4\pi/3)\rho_{AM}]^{1/3}(2E_K)^{1/2}} \quad (1)$$

(eqn. 5 of Badenes et al. 2003). The ejected mass M_{ej} and initial kinetic energy E_K are fixed by the SN Ia explosion model and the age of Tycho is well-known (431 yr). So constraints on t' correspond to constraints on the allowed ambient density ρ_{AM} . Another independent constraint on the dynamics comes from the measured angular radius of the BW, which we use below to constrain the distance to Tycho.

From Figure 9 we see that over no part of the evolution does the predicted CD:BW ratio match the observations (i.e., the green curve does not intersect the hatched region). The two other predicted ratios for this particular model do match the observations and set constraints on the allowed range of normalized time coordinate. However, these matches occur for *different* values along the normalized time coordinate. Thus the RS:BW ratio requires one range of values for the ambient density, while the RS:CD ratio requires a different, non-overlapping range of values. Clearly this model is unable to properly explain the locations of the BW, CD, and RS in a physically consistent way.

We repeated this study for the entire grid of one-dimensional hydrodynamical calculations based on the SN Ia explosion models from Badenes et al. (2003). These models cover the full range of SN Ia explosion scenarios in the literature including detonations, deflagrations, delayed detonations, pulsating delayed detonations, and sub-Chandrasekhar models. In addition we include the well-known W7 model (Nomoto et al. 1984) as well as a simple analytical exponential profile (e.g., Dwarkadas & Chevalier 1998). We use the constraints on normalized time (as in Figure 9) and the angular size of the remnant to determine the allowed range of ambient density and distance. Results are shown in Figure 10. For each

of these models, curves from the RS:BW ratio (solid curves on left) and the RS:CD ratio (dashed curves on right) do not overlap (same problem illustrated in Figure 9). The constraints provided by these ratios are physically inconsistent. These models all suffer from the same problem: *they predict that the CD is much further from the BW than we observe.*

The fact that the CD is so close to the BW while the RS remains deep in the ejecta is very puzzling. According to Wang & Chevalier (2001), Rayleigh-Taylor instabilities can produce fingers of ejecta that protrude out toward the BW with the *maximum* extent of these fingers approaching fractional radii of ~ 0.87 . This is nowhere near the value of 0.93 that we find for the *average* location of the CD.

7.3. Ejecta Clumps

Wang & Chevalier (2001) proposed that a set of high-density, high-velocity ejecta clumps in Tycho can cause the ejecta to appear to be quite close to the BW. In order to survive as distinct features near the BW at present, these clumps must have formed with a high density contrast ($\gtrsim 100$) and velocities of $\sim 7000 \text{ km s}^{-1}$ during the explosion. These authors suggest the Ni bubble effect as a plausible mechanism for forming such clumps, but detailed calculations of the process have yet to be done. If a limited number of such clumps (we find of order ten or so that protrude to the BW in projection, see Figure 4) have skewed the location of the CD to larger radii, then a more appropriate estimate for the bulk of the ejecta would exclude the clumps. We therefore also calculated the average CD radius for two angular regions with no obvious ejecta protrusions: for 203° – 270° we find the ratio of CD to BW radii to be 0.92, and for 292° – 329° we find a ratio of 0.91 (taking account of projection). These values are still too large to match the evolutionary models. Additionally, although detailed calculations of the X-ray emission have not been published, the relevant properties (temperature, ionization state, etc.) of the clumps at the edge of the SNR should differ from the bulk of the ejecta. However at least from Figure 1, we have found no obvious morphological or broadband spectral differences between the protruding ejecta and that in the interior. An upcoming article (Hughes et al. 2005) addresses the observed properties of the ejecta in Tycho. Finally this scenario explains neither the featureless nature of the blast wave spectra nor the thin rim morphology.

7.4. Cosmic Ray Acceleration

Our preferred explanation for the location of the BW, CD, and RS invokes the presence of efficient cosmic ray acceleration in Tycho. Cosmic ray acceleration at the BW would increase the compression factor there (above the usual value of 4) with a concomitant shrinking of the gap between the BW and CD (Decourchelle et al. 2000; Blondin & Ellison 2001). In particular, Blondin & Ellison (2001) state that if the compression factor is large enough, fingers of ejecta resulting from Rayleigh-Taylor instabilities at the CD can reach into the shocked interstellar medium and perturb the BW, as we observe in Tycho. In the following we divide the discussion into evidence for cosmic ray acceleration of electrons and ions at the BW, and evidence for cosmic ray acceleration at the RS.

7.4.1. Evidence for Acceleration of Electrons

If the BW in SNRs can accelerate cosmic ray *electrons* to high energies, the electrons will emit X-ray synchrotron radiation. We find two pieces of evidence for this in Tycho.

Spectra We have shown the spectra of three regions around the rim of Tycho that are *extremely* featureless (Figure 2). When fitted by an absorbed power-law model, we find photon indices ($\alpha_p \sim 2.7$) that agree with the *Ginga* best fit value. The index is similar to that found in other SNRs with non-thermal X-rays (e.g., $\alpha_p \sim 2.95$ for SN 1006, Koyama et al. 1995).

On the other hand, a thermal interpretation for the rim emission cannot be rejected based purely on spectral analysis. Hwang et al. (2002) and Bamba et al. (2005) claim that both thermal and non-thermal models provide statistically indistinguishable quality of fits to their data. To describe the rim spectra, line emission in the thermal models must be suppressed. There are two ways to accomplish this: the emitting plasma must be severely underionized or it must have very low abundances. Hwang et al. (2002) examined the former case and obtained a limit on the ionization timescale (the quantity that characterizes the ionization state of the post-shock plasma) of $n_e t \sim 10^8 \text{ cm}^{-3} \text{ s}$. This value is remarkably low and, if true, would be unprecedented. However, we can show that this scenario is internally inconsistent. Knowing the angular expansion rate of the remnant ($\sim 0.3'' \text{ yr}^{-1}$; Hughes 2000), one can determine the time it took the plasma to flow across a given post-shock distance. The interior rim regions fitted by Hwang et al. (2002) lie $\sim 5''$ in from the BW, which extrapolates to a flow time of ~ 60 yrs (with respect to the shock). The electron density therefore needs to be of order $\sim 0.05 \text{ cm}^{-3}$ to produce a very low ionization timescale.

One can also obtain an estimate of the density from the fitted normalization of the spectrum and an estimate of the emitting volume. Using our rim spectra we obtain densities in this manner of $\sim 10 (D/2.3 \text{ kpc})^{-1/2} \text{ cm}^{-3}$. The two density estimates differ by more than two orders of magnitude, which is far beyond any possible hope of redemption or accommodation by tweaking volume estimates, flow times, or other quantities.

Given the intensity of the emission, a more reasonable value for the ionization timescale would be $n_e t \sim 2 \times 10^{10} \text{ cm}^{-3} \text{ s}$. With this value fixed, we estimated the factor by which the metal abundances have to be reduced to obtain sufficient suppression of the line emission. We find that the abundances must be $< 3\%$ of the solar values in order to describe the data. Although it is possible that certain species might be depleted onto dust grains (i.e., the refractory elements like Si and Fe), neon, as it is inert, should be present in the gas phase and should produce easily visible line emission around 1 keV. All things considered a thermal interpretation for the featureless spectra at the BW in Tycho must be considered an extremely unlikely possibility.

The integrated *Ginga* spectrum of Tycho (Fink et al. 1994) shows a hard power-law component that entirely dominates the emission above ~ 15 keV. Our integrated *Chandra* spectrum over the 4–9 keV band (excluding the Fe K α line) is consistent with the extrapolation of the best-fit *Ginga* spectral model both in terms of shape and normalization (the best fit normalization from *Chandra* is only 4% higher than the quoted *Ginga* value). In this *Chandra* band, the extrapolated powerlaw component accounts for about 60% of the flux with an additional 40% coming from a thermal component (again assuming the best-fit *Ginga* spectral model). The presence of a hard featureless component in Tycho’s X-ray spectrum is thus reasonably secure. As we have argued above with the rim spectra, this hard featureless component of emission likely arises from the BW in Tycho.

Morphology Portions of the rim that show featureless spectra also show thin filaments of limb-brightened emission in the 4–6 keV band in our *Chandra* data. These features are nearly ubiquitous around the entire rim. We fit models of the predicted morphology assuming a shock-heated thermal origin for the emission profiles (see §5.2 and Figure 8). The thermal profiles cannot reproduce the sharp brightness contrast between the rim filaments and the region immediately behind the rim, while a simple projected thin shell model does provide a good fit (see §5.1 and Figure 7).

The acceleration of cosmic ray electrons gives a natural explanation for a thin emitting region: electrons will lose energy as they emit synchrotron radiation, eventually ceasing to emit X-rays. In addition, the acceleration mechanism, believed to be diffusive shock acceleration (DSA) (see e.g., Reynolds 1998, and references therein), constantly scatters

cosmic rays across the shock front. A particle scattered or advected a certain distance from the shock must diffuse back across it in order to be further accelerated. If this distance is longer than the diffusion length, the particle will lose its energy via synchrotron radiation before reaching the shock. These two effects, synchrotron losses and diffusion, combine to explain why X-ray synchrotron emission is seen in only a thin region behind the shock (for an alternate view see Pohl et al. 2005).

Since that is the case, the widths of the rims in Tycho can be used to estimate the post-shock magnetic field, B . To do this, we follow the method of Berezhko & Völk (2004), who solve a one-dimensional transport equation including diffusion, bulk flow, and loss terms to get a relation for the magnetic field:

$$B = 141 \mu\text{G} \left[\left(\frac{\Delta\theta}{2''} \right) \left(\frac{D}{2.3 \text{ kpc}} \right) \right]^{-2/3} (\sqrt{1 + \delta^2} - \delta)^{-2/3}, \quad (2)$$

where

$$\delta^2 = 0.026 \left(\frac{\sigma}{7} \right)^{-2} \left(\frac{h\nu_{max}}{5 \text{ keV}} \right)^{-1} \left[\left(\frac{p}{0.124 \% \text{ yr}^{-1}} \right) \left(\frac{D}{2.3 \text{ kpc}} \right) \left(\frac{\theta_{BW}}{243''} \right) \right]^2. \quad (3)$$

We use the average X-ray expansion rate, p , of $0.124 \% \text{ yr}^{-1}$ from Hughes (2000). Although this differs significantly from the $0.113 \% \text{ yr}^{-1}$ radio measurement of Reynoso et al. (1997), more recent radio expansion measurements (Moffett et al. 2004) indicate a rate of $0.123 \% \text{ yr}^{-1}$, in better agreement with the X-ray result. The expansion rate we use corresponds to a shock speed of $3400(D/2.3 \text{ kpc}) \text{ km s}^{-1}$. For the angular radius of the blast wave, θ_{BW} , we use the projection-corrected value of $243''$. We use a maximum photon frequency, ν_{max} , corresponding to 5 keV, since this is the middle of the 4–6 keV continuum emission used to create the rim profiles. The shock compression factor, σ , is taken to be 7, the value for a relativistic gas (the dependence on σ is weak, in any case). We use $\Delta\theta$ for the shell widths for both cases (i.e., uniform and exponential emissivity profiles). For the uniform profile widths, we find $B = 78 - 158(D/2.3 \text{ kpc})^{-0.55} \mu\text{G}$. The widths from the exponential profile give $B = 123 - 436(D/2.3 \text{ kpc})^{-0.55} \mu\text{G}$. Note that the distance scaling is approximate; the actual dependence on distance is more complicated, but these scalings are accurate for the usual range of 1.5–3 kpc. Völk et al. (2005) calculated Tycho’s magnetic field in this manner. They used widths from an exponential profile and slightly different values of p , ν_{max} , and σ . They obtained values of 150–373 μG , similar to what we find.

In the literature, there are other ways of determining the magnetic field (e.g., Vink & Laming 2003; Ballet 2005) that can be obtained from limit cases of the method presented

in Berezhko & Völk (2004). If the acceleration is efficient, then the synchrotron loss time is much longer than the time to accelerate particles to energy $E = h\nu_{max}$. In other words, particles have time to diffuse across the shock before losing energy via synchrotron radiation. In this limit we recover the method of Vink & Laming (2003):

$$B = 65.4\mu\text{G} \left[\left(\frac{\sigma}{7} \right) \left(\frac{\Delta\theta}{2''} \right) \right]^{-2/3} \left(\frac{h\nu_{max}}{5\text{keV}} \right)^{-1/3} \left[\left(\frac{p}{0.124\% \text{ yr}^{-1}} \right) \left(\frac{\theta_{BW}}{243''} \right) \right]^{2/3}. \quad (4)$$

We find $B = 33 - 66 \mu\text{G}$ for the uniform profile widths and $B = 51 - 182 \mu\text{G}$ for the exponential profile widths. This method is distance-independent. On the other hand, the acceleration time may be longer than the synchrotron loss time, and a particle will have no time to diffuse back across the shock before losing its energy via synchrotron radiation. In this limit, $\delta^2 = 0$ in eqn. 3, and we recover the method of Ballet (2005). We find the uniform profile widths yield $B = 70 - 142(D/2.3\text{kpc})^{-2/3} \mu\text{G}$, while the exponential profile widths yield $B = 110 - 392(D/2.3\text{kpc})^{-2/3} \mu\text{G}$. This method does not depend on σ . Ballet (2005) carries out this calculation for Tycho and finds $B = 250 \mu\text{G}$, using a single width from Hwang et al. (2002).

The magnetic field estimates from the uniform profile widths are consistently 1.5–2.7 times lower than estimates from the exponential profile widths. A more accurate determination of the magnetic field depends on understanding the true emissivity profile of the rim, yet we have shown that both the uniform and exponential profile models provide equally good fits to the rim emission (see §5.1). Additionally, the three methods for finding B rely on different assumptions about the synchrotron loss time compared to the time for particles to be accelerated to relativistic energies. It is beyond the scope of this paper to investigate which is most appropriate, yet it is clear further work must be done to provide accurate estimates of the magnetic field strength in SNRs. A promising avenue would be to compare the radio and X-ray rim morphologies (e.g., Ellison & Cassam-Chenaï 2005).

One possible argument against efficient cosmic ray acceleration at the forward shock of Tycho is the presence of Balmer-line filaments distributed non-uniformly around the rim in the north and east. These filaments come from non-radiative shocks propagating into a partially neutral AM (Chevalier et al. 1980). According to Draine & McKee (1993), this neutral component reduces the cosmic ray acceleration efficiency. Although most of the Balmer-line filaments do *not* appear to coincide with the 4–6 keV rim filaments, their mere existence suggests that the efficiency of cosmic ray acceleration varies around the rim of Tycho. We leave a detailed investigation of this to a future study.

7.4.2. Evidence for Acceleration of Ions

Our estimates for the post-shock magnetic field strength (see §7.4.1) in Tycho range from 33 to 436 μ G. This range comes nearly equally from three sources: (1) the different observed widths around the rim, (2) the different methods for determining these widths (uniform vs. exponential emissivity profiles), and (3) the different assumptions made about the diffusion and loss times. Making the most conservative assumptions for items (2) and (3), but considering the thinnest portion of the rim around Tycho (item 1), we find a “minimum” pre-shock magnetic field strength of \sim 10 μ G (assuming a shock compression factor of 7). This is a factor of 2 times the canonical 5 μ G value for the ISM (e.g., Ferrière 2001), which is evidence that amplification of the magnetic field is occurring at the forward shock of Tycho. Völk et al. (2005) state that such amplification can happen if a significant portion of the cosmic rays are ions.

In this article we have presented strong evidence that the CD and BW in Tycho are too close together to be described by standard adiabatic hydrodynamical models, regardless of the density or velocity structure of the SN ejecta or the evolutionary state. The closeness of the CD and BW in Tycho points to a higher compression factor for the forward shock (Ellison et al. 2005), which is then evidence for efficient cosmic ray acceleration. Since the ions dominate the mass of the fluid, these statements actually say more about the nature of the ions than the electrons. In particular, they point to the presence of relativistic ions, as we show next.

The pressure that relativistic electrons *alone* exert is insufficient to significantly alter the dynamics at the forward shock. The total available pressure at the shock can be approximated by its ram pressure, $\rho_{AM}V_{shock}^2 = 1.9 \times 10^{-7}$ erg cm $^{-3}$ (for $\rho_{AM} = 1.67 \times 10^{-24}$ g cm $^{-3}$ and $V_{shock} = 3400$ km s $^{-1}$). To have a significant affect on the dynamics, the pressure in relativistic particles should be of order \sim 50% of this ram pressure (e.g., Figure 1 of Decourchelle et al. 2000). We calculate the pressure in relativistic electrons in Tycho following the method of Longair (1994, p. 292). We use a radio spectral index of 0.61 and a flux density at 1 GHz of 56 Jy (Green 2004), our magnetic field estimates (from §7.4.1), and a distance of 2.3 kpc. Assuming the electrons fill the volume between the BW and CD, we find that the electrons provide $<0.23\%$ of the ram pressure, for any of our allowed magnetic fields. Some of the radio emission comes from the thin rims (although the bulk is from the larger volume just used), which are also where we estimated the magnetic fields. If we assume the volume of a shell of width 4'' (corresponding to the width of the thin synchrotron filaments at the rim), the relative electron pressure increases to only $<0.9\%$. This is clearly not enough to affect the dynamics of the forward shock; something else must be providing the necessary pressure.

To include cosmic ray protons in our calculations, we assumed that the energy in par-

ticles is the sum of the energies in protons and electrons, and further, that the energy in protons is some factor times the energy in electrons (Longair 1994, p. 292). For the pressure in relativistic particles to be 50% of the ram pressure, the energy density in protons must be ≥ 50 times the energy density in electrons. This is the most conservative estimate, using our lowest magnetic field value ($33 \mu\text{G}$) and the volume of a shell of width $4''$. Taken together with the evidence for high energy relativistic electrons at the BW in Tycho there is now a compelling case for cosmic ray acceleration of *both* ions and electrons at the forward shock in Tycho. We further note the broad consistency between our estimate of the ratio of proton to electron energy densities in Tycho and the well-established value for Galactic cosmic rays of ~ 100 (Longair 1994, p. 307).

7.4.3. Evidence for Acceleration at the Reverse Shock

Some authors have proposed that the RS can also accelerate cosmic rays. If this occurs, then the gap between the RS and CD will also shrink (Decourchelle et al. 2000). However, our results argue against a significant increase in the compression factor at the RS. The observed gap between the RS and CD is rather large. Ellison et al. (2005) have investigated particle acceleration at the RS and find that increased compression factors there result in much lower post-shock temperatures than in the case with no acceleration. They state that this prediction is a problem for SNRs with strong Fe K α lines, as we see in Tycho. These authors also point out that particle acceleration at the reverse shock in remnants of Type Ia SNe is expected to be negligible unless the original magnetic field of the progenitor white dwarf was unusually large or amplification of the field occurred subsequently. Additionally, Decourchelle et al. (2000) fit models to the spectrum of Kepler's SNR and found a good fit for cosmic ray acceleration at the BW, but no acceleration at the RS. This is consistent with our findings for Tycho.

8. Summary

We have used the relative locations of the forward shock, contact discontinuity, and reverse shock to argue for efficient cosmic ray acceleration at Tycho's forward shock. The ratio of the CD to BW radii (0.93) is inconsistent with adiabatic hydrodynamical models, even when Rayleigh-Taylor instabilities are taken into account. The closeness of the CD and BW are consistent with a scenario in which the forward shock is efficiently accelerating cosmic ray ions. This causes the shock compression factor to increase, and the gap between the CD and BW to shrink. Evidence for the acceleration of cosmic ray electrons to TeV

energies comes from the interpretation of the spectrally featureless rim as nonthermal X-ray synchrotron emission. A modest fraction ($\sim 40\%$) of the 4–6 keV continuum emission observed by *Chandra* from the entire remnant is thermal and it is possible that most of this is associated with the prominent thermally-emitting ejecta. At the rim, the fraction of 4–6 keV emission that can be thermal is much smaller, $\sim 10\%$. In fact the non-thermal interpretation by itself can explain the spectrum and morphology of the rim and a 2 keV thermal model is not required.

The question then arises: since the ambient density around Tycho cannot be exceptionally low, where is the thermal emission from the blast wave? Based on our work (and also noted by Hwang et al. 2002) the electron temperature of the blast wave must be less than 2 keV. In the literature there is one measurement of the proton and electron temperatures at the rim of Tycho’s SNR from the optical Balmer line emission of knot “g” at the eastern limb (Ghavamian et al. 2001). These authors find a post-shock proton temperature of $\sim 10^8$ K and an electron temperature of $< 10^7$ K (< 0.9 keV) (although their models assume negligible cosmic ray acceleration). If the average electron temperature around the rim of Tycho is comparable to or somewhat less than this value, its X-ray emission will be absorbed by the ISM and therefore largely invisible to us. Thus the rim of Tycho’s SNR may be similar to other remnants, such as G347.3–0.5, in which the X-rays appear to be purely nonthermal with no detectable thermal emission present (Slane et al. 1999). In cases like these, where information from the thermal plasma is lacking, other tracers of the dynamical state of the remnant, such as expansion rates, locations of the fluid discontinuities, and proton/electron temperatures measured from Balmer-line filaments, become that much more precious.

For years, astronomers have been estimating explosion energies, ages, and ambient densities for young SNRs based on the observed properties of the forward shock under the assumption of adiabatic dynamics (e.g., Sedov-Taylor, Truelove & McKee 1999). As we have shown here, the dynamics of the forward shock in Tycho are dominated by efficient cosmic ray acceleration. If Tycho is a typical case, then all these previous estimates are based on incorrect assumptions. Future work needs to concentrate on improving model assumptions, determining how common the cosmic-ray-acceleration-dominated phase is and constraining its duration in order to arrive at a better understanding of the relationship between SNe and SNRs, SNR evolution, and the influence they have on galactic environments.

JPH acknowledges support from the International Space Science Institute in Bern, Switzerland, which facilitated fruitful discussions with Anne Decourchelle, Don Ellison, and other colleagues on topics related to the work presented here. We thank David Burrows and John Nousek for assistance with the original proposal, as well as Ken Nomoto for the use of his W7 model and Jacco Vink for a helpful discussion about magnetic field estimates.

CFM acknowledges support from NSF grant AST00-98365 and from the Miller Foundation for Basic Research. Support for this work was provided by the National Aeronautics and Space Administration through *Chandra* Award Number GO3-4066X issued to Rutgers by the *Chandra X-ray Observatory* Center, which is operated by the Smithsonian Astrophysical Observatory for and on behalf of the National Aeronautics Space Administration under contract NAS8-03060.

REFERENCES

Allen, G. E. et al. 1997, *ApJ*, 487, L97

Badenes, C., Borkowski, K. J., & Bravo, E. 2005, *ApJ*, 624, 198

Badenes, C., Bravo, E., Borkowski, K. J., & Domínguez, I. 2003, *ApJ*, 593, 358

Ballet, J. 2005, COSPAR, Plenary Meeting, 765

Bamba, A., Yamazaki, R., Yoshida, T., Terasawa, T., & Koyama, K. 2005, *ApJ*, 621, 793

Baring, M. G., Ellison, D. C., & Slane, P. O. 2005, COSPAR, Plenary Meeting, 2066

Baron, E., Lentz, E. J., & Hauschildt, P. H. 2003, *ApJ*, 588, L29

Berezhko, E. G. & Völk, H. J. 2004, *A&A*, 419, L27

Blondin, J. M. & Ellison, D. C. 2001, *ApJ*, 560, 244

Borkowski, K. J., Lyerly, W. J., & Reynolds, S. P. 2001, *ApJ*, 548, 820

Bravo, E., Badenes, C., & García-Senz, D. 2004, astro-ph/0412155

Chevalier, R. A., Blondin, J. M., & Emmering, R. T. 1992, *ApJ*, 392, 118

Chevalier, R. A., Kirshner, R. P., & Raymond, J. C. 1980, *ApJ*, 235, 186

Decourchelle, A., Ellison, D. C., & Ballet, J. 2000, *ApJ*, 543, L57

Decourchelle, A. et al. 2001, *A&A*, 365, L218

Dickel, J. R., van Breugel, W. J. M., & Strom, R. G. 1991, *AJ*, 101, 2151

Draine, B. T., & McKee, C. F. 1993, *ARA&A*, 31, 373

Dwarkadas, V. V. & Chevalier, R. A. 1998, *ApJ*, 497, 807

Ellison, D. C. 2001, *SSRv*, 99, 305

Ellison, D. C., & Cassam-Chenaï, G. 2005, *ApJ*, in press (astro-ph/0507031)

Ellison, D. C., Decourchelle, A., & Ballet, J. 2005, *A&A*, 429, 569

Ferrière, K. M. 2001, *Reviews of Modern Physics*, 73, 1031

Fink, H. H., Asaoka, I., Brinkmann, W., Kawai, N., Koyama, K. 1994, *A&A*, 283, 635

Gamezo, V. N., Khokhlov, A. M., Oran, E. S., Chtchelkanova, A., & Rosenberg, R. 2003, *Science*, 299, 77

García-Senz, D. & Bravo, E. 2005, *A&A*, 430, 585

Ghavamian, P., Raymond, J., Smith, R. C., & Hartigan, P. 2001, *ApJ*, 547, 995

Green, D. A. 2004, *Bulletin of the Astronomical Society of India*, 32, 335

Hamilton, A. J. S., Sarazin, C. L., & Szymkowiak, A. E. 1986, *ApJ*, 300, 713

Hillebrandt, W. & Niemeyer, J. C. 2000, *ARA&A*, 38, 191

Hughes, J. P. 2000, *ApJ*, 545, L53

Hughes, J. P., Rakowski, C. E., & Decourchelle, A. 2000, *ApJ*, 543, L61

Hughes, J. P. et al. 2005, *ApJ*, in prep.

Hwang, U., Decourchelle, A., Holt, S. S., & Petre, R. 2002, *ApJ*, 581, 1101

Hwang, U. & Gotthelf, E. V. 1997, *ApJ*, 475, 665

Hwang, U., Hughes, J. P. & Petre, R. 1998, *ApJ*, 497, 833

Katz-Stone, D. M., Kassim, N. E., Lazio, T. J. W., & O'Donnell, R. 2000, *ApJ*, 529, 453

Koyama, K., Petre, R., Gotthelf, E. V., Hwang, U., Matsuura, M., Ozaki, M., & Holt, S. S. 1995, *Nature*, 378, 255

Longair, M. S. 1994, *High Energy Astrophysics*, Vol. 2 (2nd ed.; Cambridge: Cambridge Univ. Press)

Malkov, M. A., Diamond, P. H., & Sagdeev, R. Z. 2005, *ApJ*, 624, L37

Moffett, D., Caldwell, C., Reynoso, E., & Hughes, J. P. 2004, in *IAU Symp. 218, Young Neutron Stars and Their Environments*, ed. F. Camilo & B. Gaensler (San Francisco: ASP), 69

Murtagh, F. & Heck, A. 1987, *Multivariate Data Analysis* (Dordrecht, Holland: D. Reidel Publishing Co.)

Nomoto, K., Thielemann, F.-K., & Yokoi, K. 1984, *ApJ*, 286, 644

Pohl, M., Yan, H., & Lazarian, A. 2005, *ApJ*, 626, L101

Reinecke, M., Hillebrandt, W., & Niemeyer, J. 2002, *A&A*, 391, 1167

Reynolds, S. P. 1998, *ApJ*, 493, 375

Reynolds, S. P. & Ellison, D. C. 1992, *ApJ*, 399, L75

Reynoso, E. M., Moffett, D. A., Goss, W. M., Dubner, G. M., Dickel, J. R., Reynolds, S. P., & Giacani, E. B. 1997, *ApJ*, 491, 816

Seward, F., Gorenstein, P., & Tucker, W. 1983, *ApJ*, 266, 287

Slane, P., Gaensler, B. M., Dame, T. M., Hughes, J. P., Plucinsky, P. P., & Green, A. 1999, *ApJ*, 525, 357

Slane, P., Hughes, J. P., Edgar, R. J., Plucinsky, P. P., Miyata, E., Tsunemi, H., & Aschenbach, B. 2001, *ApJ*, 548, 814

Smith, R. C., Kirshner, R. P., Blair, W. P., & Winkler, P. F. 1991, *ApJ*, 375, 652

Truelove, J. K. & McKee, C. F. 1999, *ApJS*, 120, 299

Vancura, O., Gorenstein, P., & Hughes, J. P. 1995, *ApJ*, 441, 680

Velázquez, P. F., Gómez, D. O., Dubner, G. M., Giménez de Castro, G., & Costa, A. 1998, *A&A*, 334, 1060

Vink, J. & Laming, J. M. 2003, *ApJ*, 584, 758

Völk, H. J., Berezhko, E. G., & Ksenofontov, L. T. 2005, *A&A*, 433, 229

Wang, C.-Y., & Chevalier, R. A. 2001, *ApJ*, 549, 1119

Warren, J. S., & Hughes, J. P. 2005, *ApJ*, in prep.

Table 1. Energy Bands used for PCA

Number	Energy Range (keV)	Feature
1	0.50–0.70	O
2	0.70–0.95	Fe L
3	0.95–1.26	Fe L/Ne
4	1.26–1.43	Mg/Fe L
5	1.43–1.63	continuum
6	1.63–2.26	Si K
7	2.26–2.96	S K
8	2.96–3.55	Ar K
9	3.55–4.10	Ca K
10	4.10–6.10	continuum
11	6.10–6.80	Fe K
12	6.80–9.00	continuum/background

Note. — Features listed are general, and only possible (not necessarily detected) for that energy range.

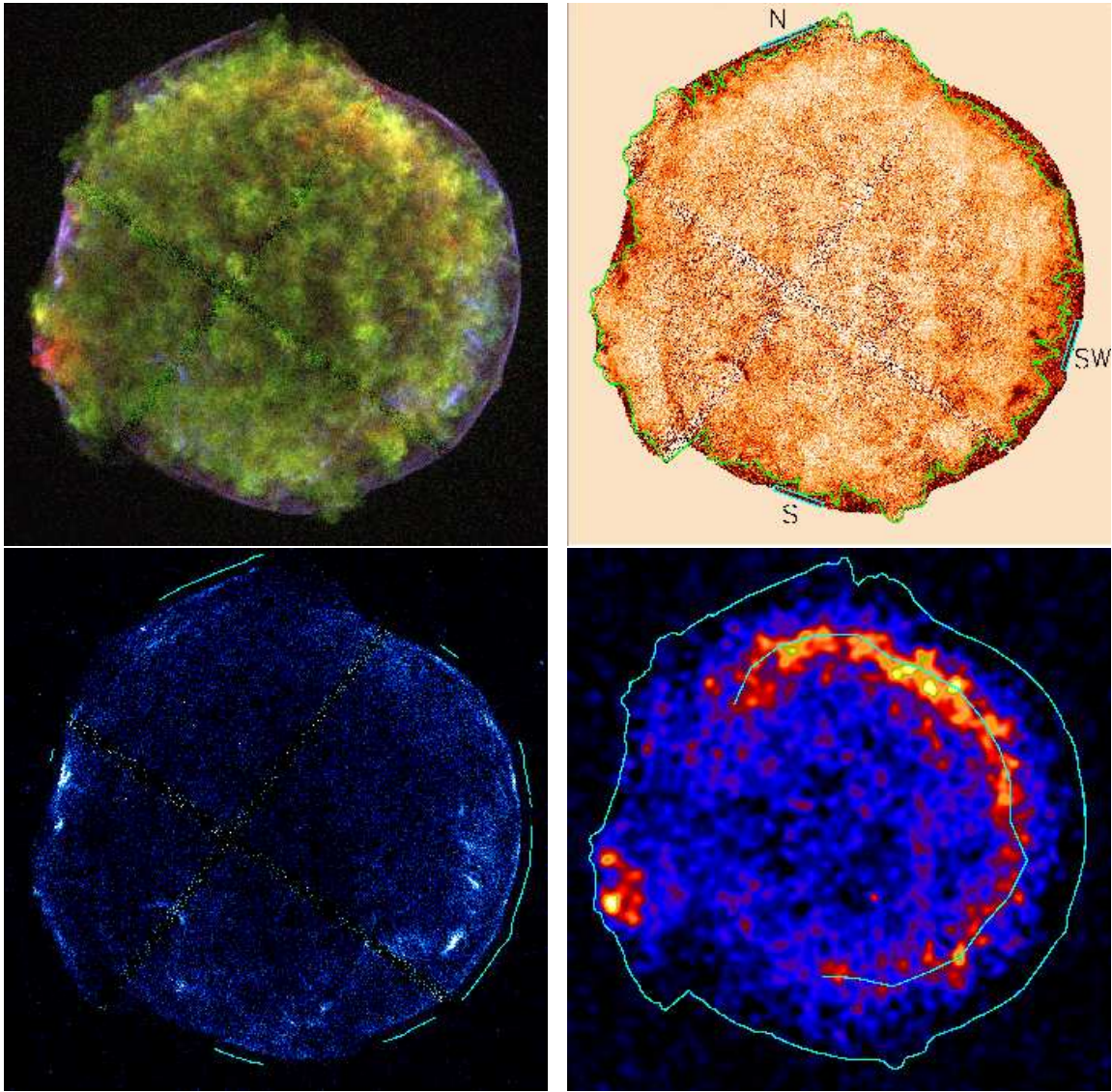


Fig. 1.— *Top left*: Three-color composite *Chandra* image of Tycho's SNR. The red, green, and blue images correspond to photon energies in the 0.95–1.26 keV, 1.63–2.26 keV, and 4.1–6.1 keV bands, respectively. *Top right*: An image of the first principal component (PC1) that separates line-rich emission (light regions) from featureless emission (dark regions). The green contour indicates the location of the contact discontinuity. Three spectral extraction regions are indicated. *Bottom left*: Continuum (4–6 keV band) image with regions used to determine width of rim filaments indicated. *Bottom right*: Fe K α line image with continuum (4–6 keV band) subtracted. The inner contour notes the location of the reverse shock and the outer contour the location of the blast wave. The field of view of each panel is 9.5' \times 9.5'. North is up and east is to the left.

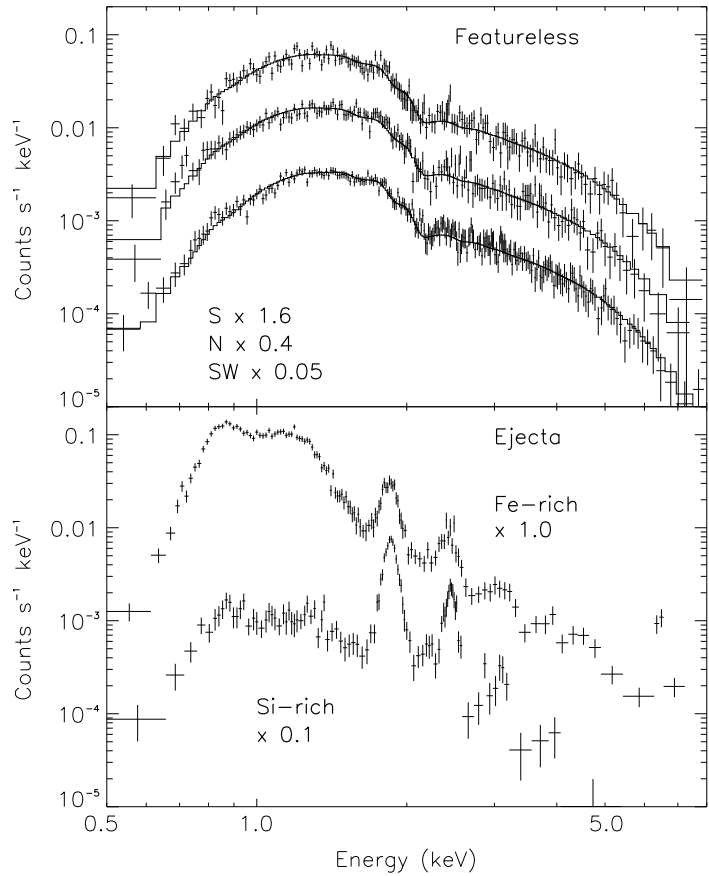


Fig. 2.— *Top:* Spectra and best fit models for featureless emission. *Bottom:* Spectra for ejecta emission. The Fe-rich spectrum is from the reddish region in the southeast, and the Si-rich region is from the yellowish region in the southeast.

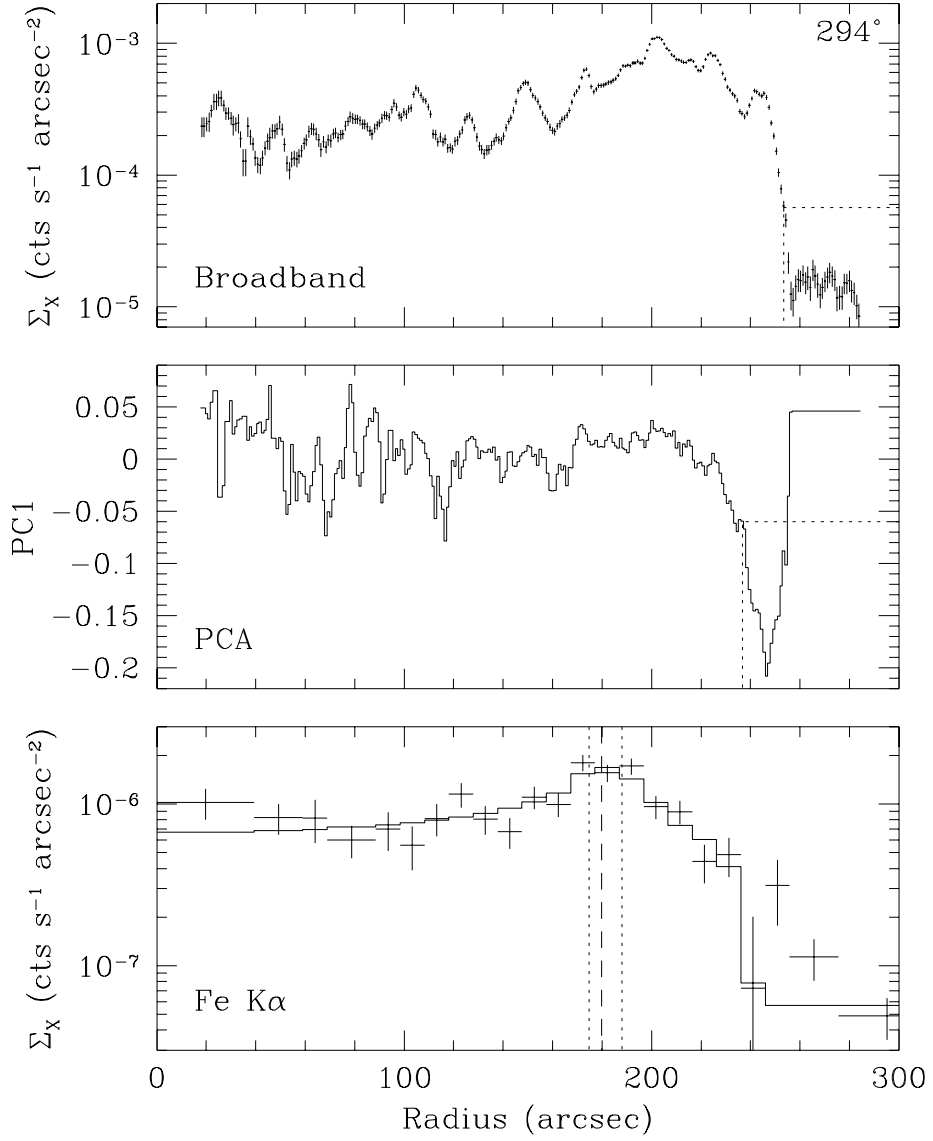


Fig. 3.— Radial surface brightness profiles for a wedge centered at 294° , measured counter-clockwise from north. *Top*: Broadband emission. The dashed lines indicate the contour level chosen to mark the blast wave (5.7×10^{-5} $\text{cts s}^{-1} \text{arcsec}^{-2}$) and the corresponding radius. *Middle*: PC1 values. The dashed lines indicate the threshold chosen to mark the contact discontinuity (-0.06) and the corresponding radius. *Bottom*: Fe K α emission with continuum subtracted. The crosses are the data and the solid histogram is the best-fit thin shell model. The dashed vertical line marks the location of the inner edge of the best-fit thin shell model and the two dotted lines show the $1-\sigma$ allowed range.

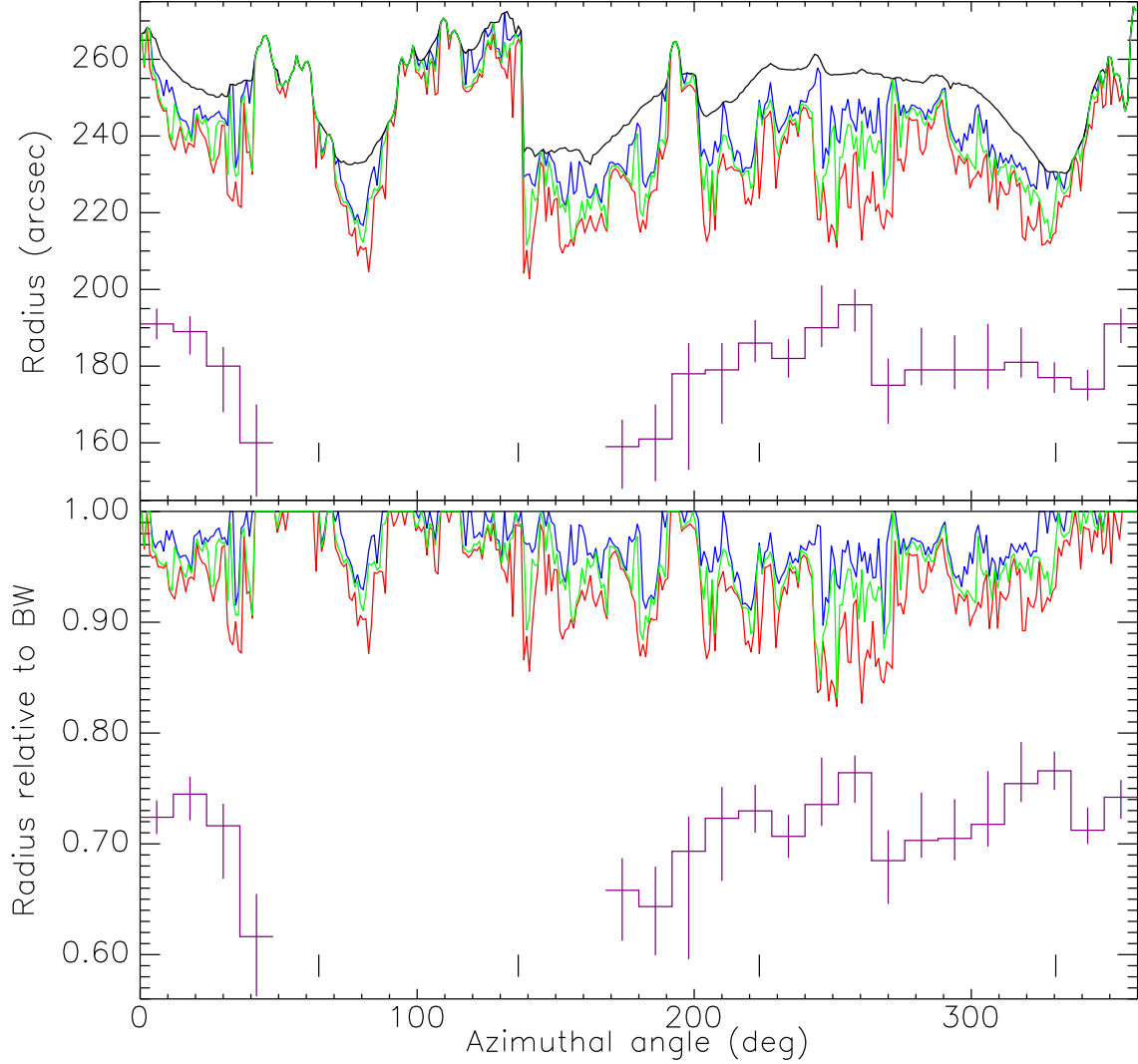


Fig. 4.— *Top*: Radius of the blast wave (BW, black), contact discontinuity (CD, 2- σ : red, 3- σ : green, 4- σ : blue), and reverse shock (RS, purple) versus azimuthal angle for Tycho’s SNR. The error bars on the RS are 90%. The four small vertical tic marks near the bottom of the figure indicate where the gaps between the four ACIS-I CCD chips lie. North corresponds to 0° and angles increase counterclockwise. *Bottom*: As in the top panel, with ratio of CD to BW and RS to BW plotted versus azimuthal angle.

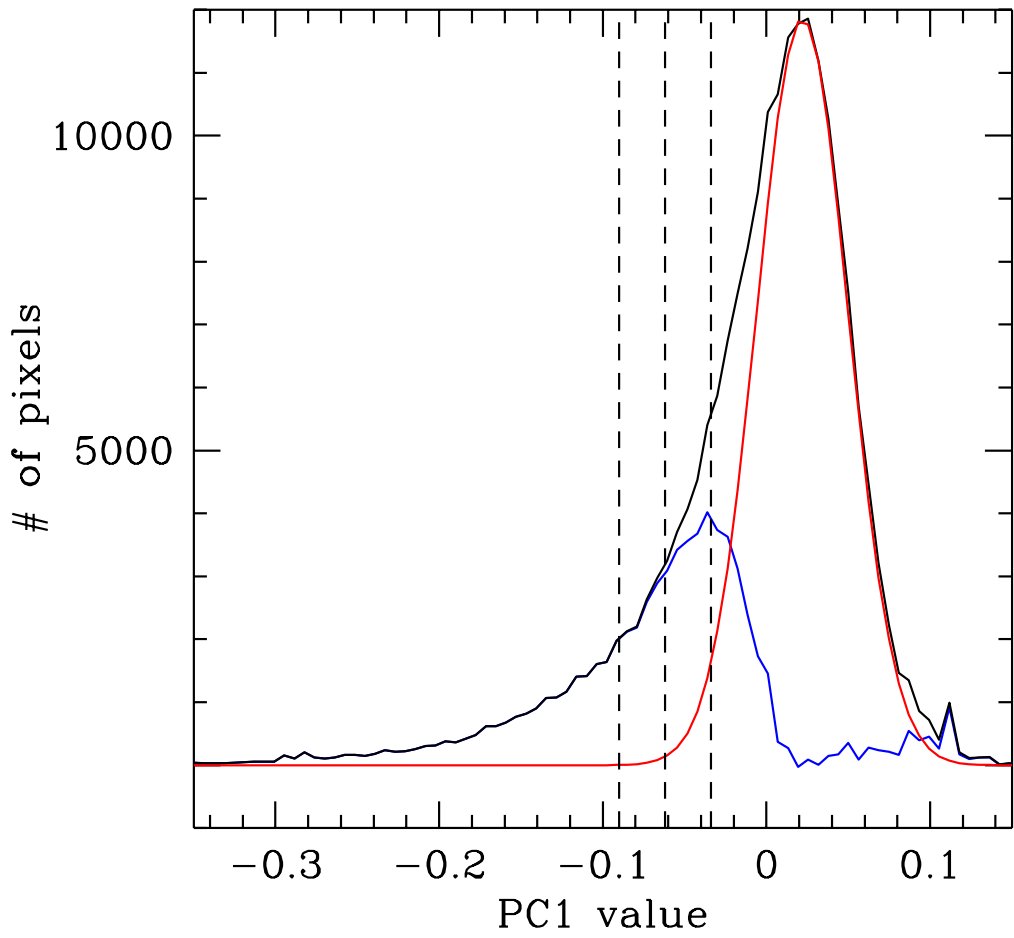


Fig. 5.— Distribution of PC1 values (black) overlaid with best-fit Gaussian (red, $\sigma=0.028$), which represents the pixels with thermal spectra. The difference between these two is shown in blue, and the dashed lines mark PC1 values 2σ , 3σ , and 4σ away from the peak of the Gaussian.

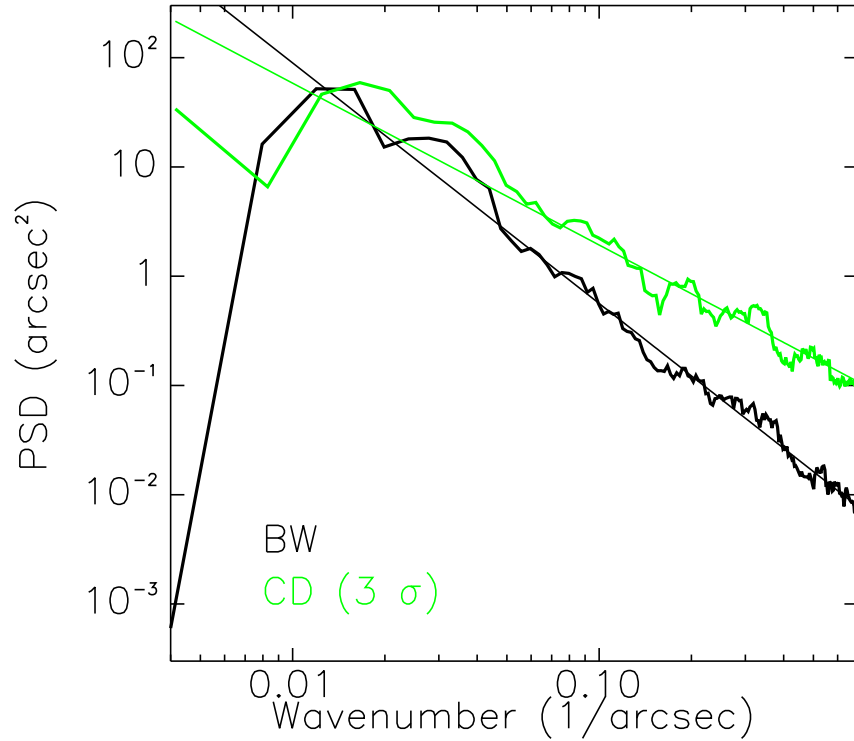


Fig. 6.— Power spectrum of radius fluctuations from Figure 4 versus wavenumber for the blast wave (BW) and contact discontinuity (CD). Each case is well described by a power law as plotted.

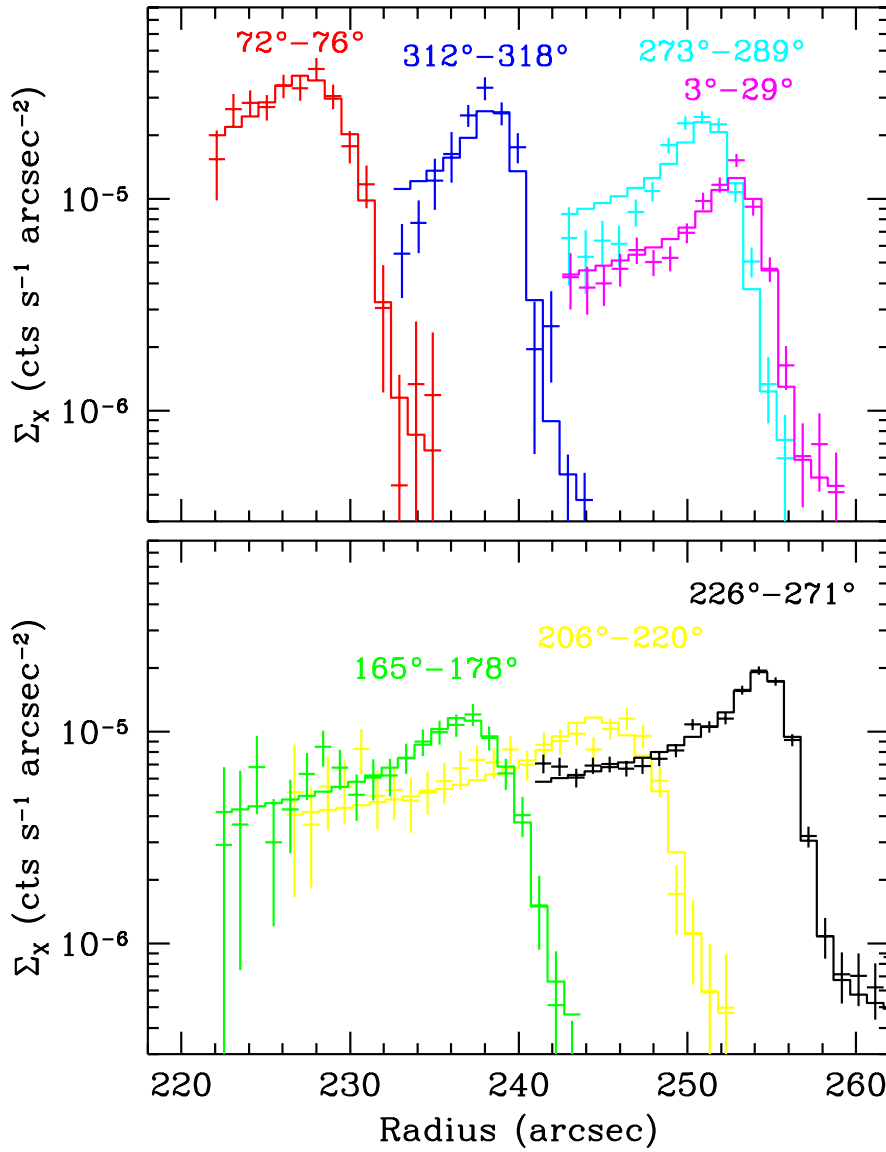


Fig. 7.— Radial surface brightness profiles in the 4–6 keV band for seven regions around the rim. The histogram overlaid on each profile is the best-fit geometrically-thin uniform-emissivity spherical shell model. North corresponds to 0° and angles increase counterclockwise.

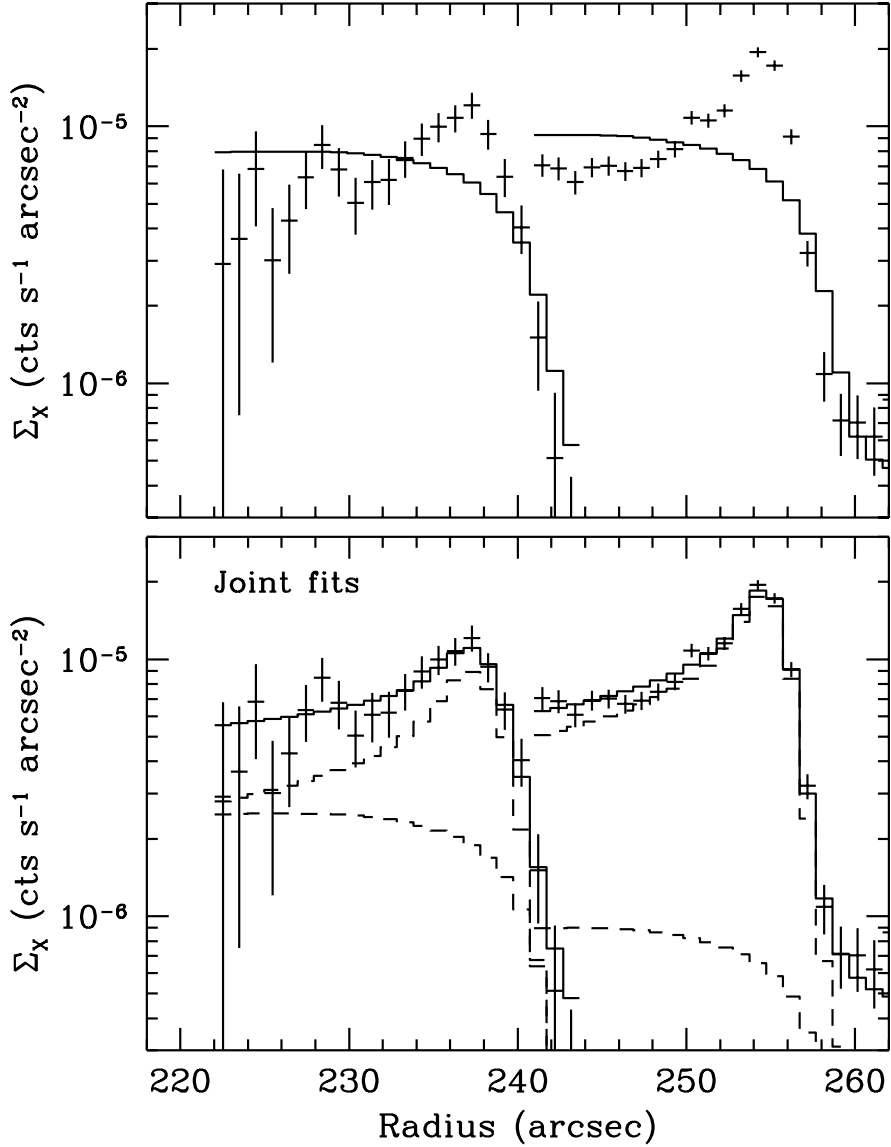


Fig. 8.— Radial surface brightness profiles in the 4-6 keV band for two selected regions around the rim (azimuthal angles 165° – 176° on the left and 226° – 271° on the right). *Top*: The histogram overlaid on each profile is the best-fit model of thermal emission from shocked ambient medium based on our 1D hydrodynamic and ionization calculations. *Bottom*: The solid histogram is the joint model of a geometrically-thin uniform-emissivity spherical shell and the thermal shocked plasma model. The dashed histograms show the contributions from the two cases separately. This is not the best fit, but rather the upper limit (90% confidence) allowed by the data for the thermal shocked plasma model.

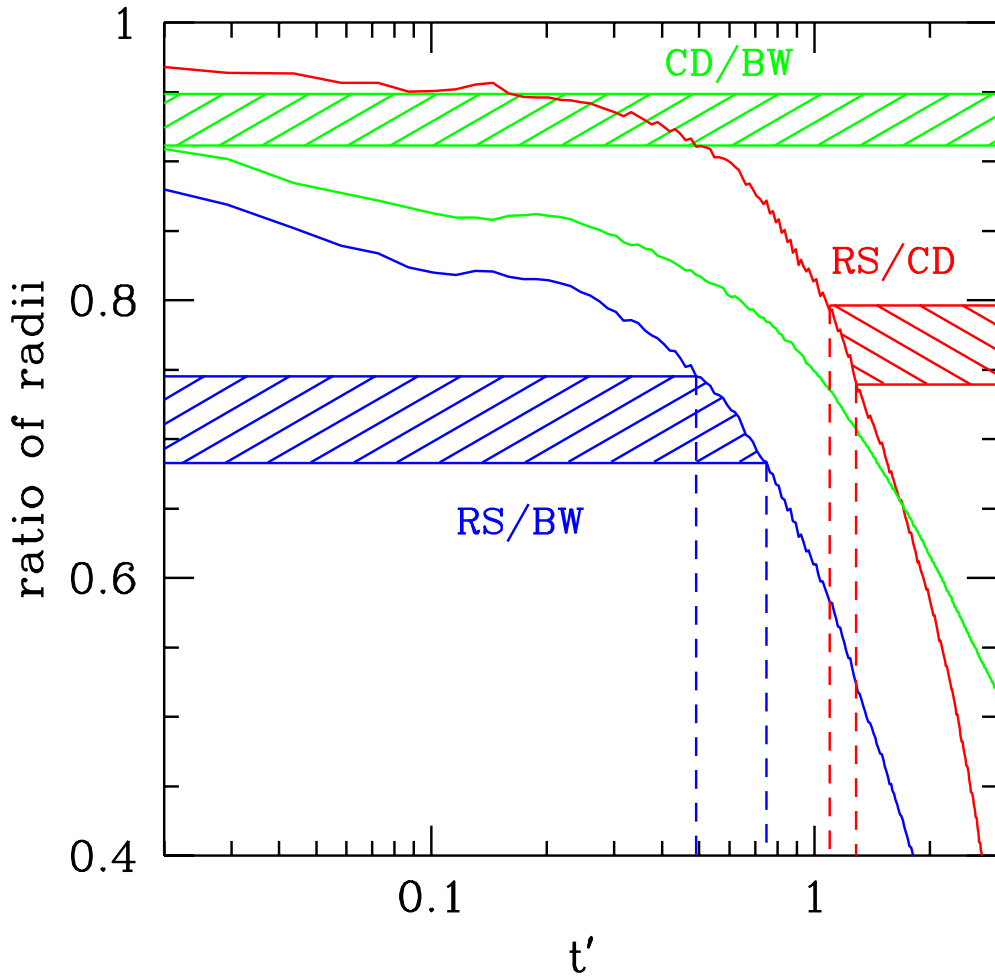


Fig. 9.— Time evolution of the various ratios of radii for the BW, CD, and RS as labelled. The horizontal axis corresponds to time in normalized units. The curves are from a 1-D hydrodynamical calculation (model DDTc from Badenes et al. 2005) and the cross-hatched bands show the allowed ranges from our analysis of Tycho’s SNR.

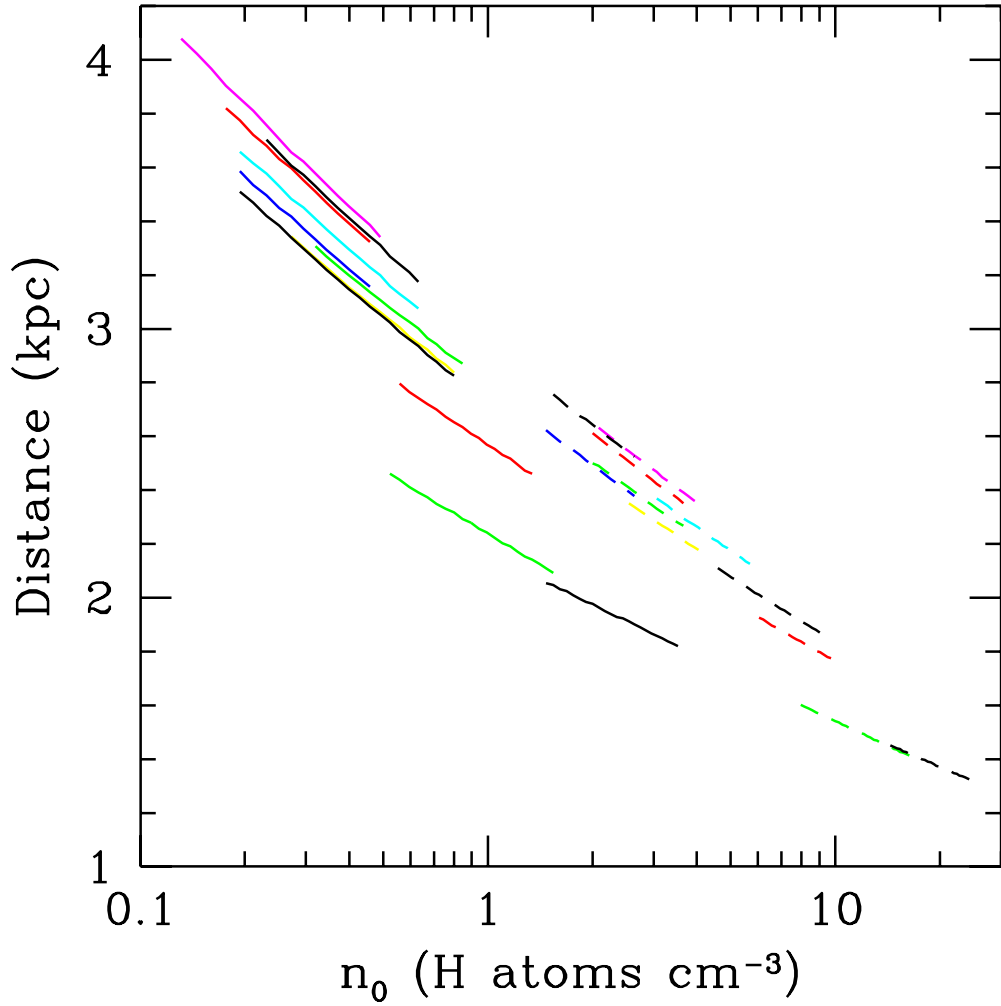


Fig. 10.— Distance vs. ambient density estimates for Tycho’s SNR from a variety of SN Ia explosion models. Each model provides a range of allowed values for distance vs. ambient density that are consistent with the observed limits on the ratio of RS:BW radii (solid curves on left) or the ratio of RS:CD radii (dashed curves on right). The different colors correspond to different models; for our purposes it is not necessary to distinguish between them, since in no case do the allowed ranges overlap.